

Cite this: *J. Mater. Chem. C*, 2019,
7, 8803Received 3rd June 2019,
Accepted 8th July 2019

DOI: 10.1039/c9tc02974e

rsc.li/materials-c

Advancing next generation nanolithography with infiltration synthesis of hybrid nanocomposite resists†

Nikhil Tiwale,^a Ashwanth Subramanian,^b Kim Kisslinger,^a Ming Lu,^a
Jiyoung Kim,^c Aaron Stein^a and Chang-Yong Nam^{b*}

Organic–inorganic hybrid resists are emerging as an effective way of addressing stringent process requirements for aggressive down-scaling of semiconducting devices. However, hybrid resists generally require complex chemical synthesis while being predominantly negative-tone with high dose requirements. For positive-tone processes and high-aspect-ratio pattern transfers, resist choices are limited to costly, non-hybrid alternatives, whose etch resistance is still inferior compared with hybrid resists. Here, we demonstrate a novel hybrid positive-tone resist platform utilizing simple *ex situ* vapor-phase inorganic infiltration into standard resist materials. A model system based on poly(methyl methacrylate) (PMMA) thin film hybridized with aluminum oxide has been demonstrated for electron-beam lithography patterning, featuring a fully controllable critical exposure dose, contrast, and etch resistance. The hybrid resist not only achieves contrast as high as ~ 30 , six-fold enhancement over standard PMMA, but also enables Si nanostructures with resolution down to ~ 30 nm and an aspect ratio as high as ~ 17 , owing to enhancement of the Si etch selectivity to ~ 70 , with an estimated achievable maximum of ~ 300 , far exceeding known commercial positive-tone resist systems. The easy implementability, combined with versatile *ex situ* control of resist characteristics, makes this hybrid resist synthesis approach uniquely suited for addressing the resist performance and high throughput required for advanced nanolithography techniques, such as extreme ultraviolet lithography, potentially.

Introduction

Lithography has played a crucial role in the gigantic processing power that the semiconductor industry has conjured by shrinking down electronic device feature sizes to the sub-10 nm length scale.

So far, the photoresists that allowed reproducible fabrication of such small length-scale devices have been largely carbon-based, chemically amplified resists (CAR). However, more recently, organic–inorganic hybrid resists are gaining significant attention, in order to satisfy the stringent requirements imposed by the aggressive device-scaling.¹ Until now, industry-scale lithography has been dependent on 193 nm immersion lithography (193-i),² with further scaling imparted by clever engineering tricks such as directed self-assembly^{3,4} and multi-patterning.^{1,5} Lithography techniques capable of directly patterning sub-10 nm-scale resolution such as electron beam lithography (EBL) and extreme ultraviolet (EUV) lithography are currently being pursued for application in high-volume manufacturing (HVM). However, in order to transfer these high-resolution patterns into required substrates with high aspect ratios, hybrid resists must provide a key solution.^{1,6}

Performance of a lithographic tool inevitably depends on the resists capable of instilling the required nanopatterns. To this end, the currently existing resists face a number of challenges. Typically, at the resist thicknesses that have been used for previous technology nodes, the high-resolution patterns undergo pattern collapse, necessitating a decrease in the resist thickness, where such small linewidths could be realized.⁷ Consequently, the resist patterns do not survive the plasma-etch time required to transfer them into the substrate with the required high aspect ratio.¹ In order to balance the resolution-etch selectivity trade-off, thin layer imaging (TLI) and related approaches have been exploited, such as top surface imaging (TSI) *via* silylation,^{8–16} use of bilayer resists consisting of a Si-containing top layer,¹⁷ selective area atomic layer deposition (ALD),¹⁸ ion beam implantation,^{19–21} and a hard mask underlayer.¹⁷ Nowadays, multilayer stacks are in use to increase the pattern transfer selectivity, but their implementation requires multiple processing steps which negatively affects the throughput and cost.

Hybrid resists offer an elegant solution over this conundrum. The increased mechanical strength due to the inorganic component helps in reducing the pattern collapse. Moreover, the enhanced robustness, imparted by the inorganic entities, provides a higher etch resistance allowing a deep, high-aspect-ratio etching

^a Center for Functional Nanomaterials, Brookhaven National Laboratory, Upton, New York 11973, USA. E-mail: cynam@bnl.gov

^b Department of Materials Science and Chemical Engineering, Stony Brook University, Stony Brook, New York 11794, USA

^c Department of Materials Science and Engineering, University of Texas at Dallas, Richardson, Texas 75080, USA

† Electronic supplementary information (ESI) available. See DOI: 10.1039/c9tc02974e

into the substrate. In addition, for EUV lithography, where the absorption of the EUV radiation primarily takes place at the atomic level, inclusion of specific elements into the resist matrix can improve the energy absorbed by the resist and, thus, the throughput.¹ To this end, a number of inorganic-entity containing hybrid resist strategies are being actively investigated for EUV resist applications, such as those based on nanoparticles,^{6,22–27} oxalates,^{28–31} and oxocages.^{32,33}

One of the seminal works on metal-containing electron beam (e-beam) resists was conducted by Webb and Hatzakis of IBM using metal methacrylates.³⁴ However, this approach has remained a relatively unpopular choice because of the high exposure dose necessary to generate solubility contrast. Another early approach of incorporating an inorganic entity into the resist utilized a copolymer of methyl methacrylate (MMA) and 3-triethoxysilylpropyl methacrylate (ESPMA). Only 1–10% addition of ESPMA leads to 4–10 times improvement of the etch resistance.³⁵ Saifullah and Welland *et al.* investigated e-beam resists containing a number of metals and associated metal oxides based on Al, Ti, Hf, Zr, Zn, Ni, and Cu.^{36–45} While an excellent linewidth resolution was demonstrated, their sensitivity was extremely low, thus requiring a high exposure dose for generating the patterns. Greci, Zanchetta, Brusatin *et al.* have demonstrated a highly etch-resistant molecular resist (containing organo-phenylsilane derivatives) with a moderate exposure dose,^{46–49} which was later also co-opted by Cattoni *et al.* using less toxic silane derivatives.⁵⁰ Despite demonstrating Si etch selectivity up to 100:1 for this resist system, susceptibility of the silane group to ambient humidity poses limitations on their long-term shelf-life.⁵⁰ More recent works have tried to utilize resists containing metal peroxide sulfates,^{51,52} metal sulfonates,⁵³ metal containing polymers (MCP)⁵⁴ and organosilicates.^{55,56} Hydrogen silsesquioxane (HSQ), a Si-containing caged monomer-based resist, has been the most widely used inorganic based resist for EBL. However, similar to most hybrid resists, HSQ is also a negative-tone resist with a high exposure dose requirement.^{57–60} Moreover, most of these hybrid resists are chemically synthesized using processes that would require a highly skilled workforce. These resists are also generally hard to remove and leave behind residue after lithography.

Meanwhile, there are only a few variants of positive-tone e-beam resists with a high etch resistance that have been explored. The most popularly employed resist choices for plasma etch based patterning include copolymer resists such as ZEP520A (Zeon Corp.),^{61,62} CSAR62 (ALLRESIST GmbH)^{63,64} or a photoacid generator (PAG) containing the CAR-UV series (Shipley/Dow Chemical).⁶⁵ It must be noted that all these resists have proprietary compositions with a relatively high associated cost. While these resists show moderately improved etch resistance, being inherently organic, they still suffer from typical limitations of carbon-based resists detailed earlier. To this end, the reports of positive-tone, metal containing hybrid resists are particularly lacking.

In this study, we demonstrate a novel hybrid positive-tone e-beam resist system, developed entirely using readily available standard material systems and fabrication tools. Our process

does not involve any kind of complex chemical synthesis, making it easy to implement with custom protocols. Moreover, since our resist system is based on existing resist materials with *ex situ* processing used to modify the resist prior to exposure, issues such as substrate adhesion, which may occur with resists synthesized by complex chemistry, are completely avoided; whereas, since *ex situ* processing requires only standard fabrication tools, the same principles can be easily implemented for other metals and metal oxides to achieve specific performance. A key novelty in our resist system is the inherent controllability of various resist parameters, such as sensitivity (D_{50}), contrast (γ) and plasma etch resistance, as per the need of the user and the end application. Within this resist platform, we report hybrid nanocomposite resists with contrast, γ , ranging from 2 to 30 by carefully controlling the amount of inorganic entity (AlO_x). Using our hybrid resist with thickness as small as ~ 60 nm, we were able to etch Si features down to ~ 30 nm linewidth and a very high aspect ratio of ~ 17 . The etch selectivity of the corresponding resist formulation for cryogenic Si etching was estimated to be as high as ~ 70 , which is a fourteen-fold increase in the etch selectivity of the original (pre-hybridization) organic resist and even over five-fold higher than the resist of choice for etch processes, ZEP. Based on measured etch rates of resists infiltrated with a higher number of infiltration cycles, we also estimate the selectivity in excess of 300.

Poly(methyl methacrylate), more commonly known as PMMA, is by far the most widely used EBL resist.^{66–71} Its popularity, in part, stems from the associated simple nature of the chemistry involved and its ubiquitous, low-cost availability as well as its long-term shelf life. It is a positive-tone resist, which has also been demonstrated to show ~ 1 nm patterning resolution, the highest resolution reported for any EBL resist.⁷² However, one major negative side for the conventional PMMA resist is that it lacks plasma etch resistance,⁷³ which has led the EBL users to rather costly alternative resists such as ZEP and CSAR. Our PMMA-based hybrid resist tackles this very drawback with a low-cost synthesis technique. Even in the semiconductor industry, which has been heavily dependent on 193-i lithography, copolymers of methacrylate derivatives have been the workhorse for HVM.^{2,74–76} Consequently, the hybridized resist system reported here can have a lasting impact by easily adopting it for a number of different advanced lithography techniques.

We have employed a recently developed vapor-phase hybridization technique called infiltration synthesis or vapor-phase infiltration.^{77–79} The technique utilizes an ALD system, a very common thin-film deposition equipment found in almost every micro-nano-fabrication facility. The substrate is first coated with the required thickness of the PMMA resist using a simple spin-coating technique and then loaded into the ALD chamber maintained at a moderate temperature (85°C), below the glass transition temperature of PMMA. During the infiltration process, Al precursor, trimethylaluminum (TMA), is first introduced into the chamber for a stipulated amount of time while the chamber is isolated from the pump. At the end of the required time, TMA is then purged out of the chamber. This constitutes the first half of

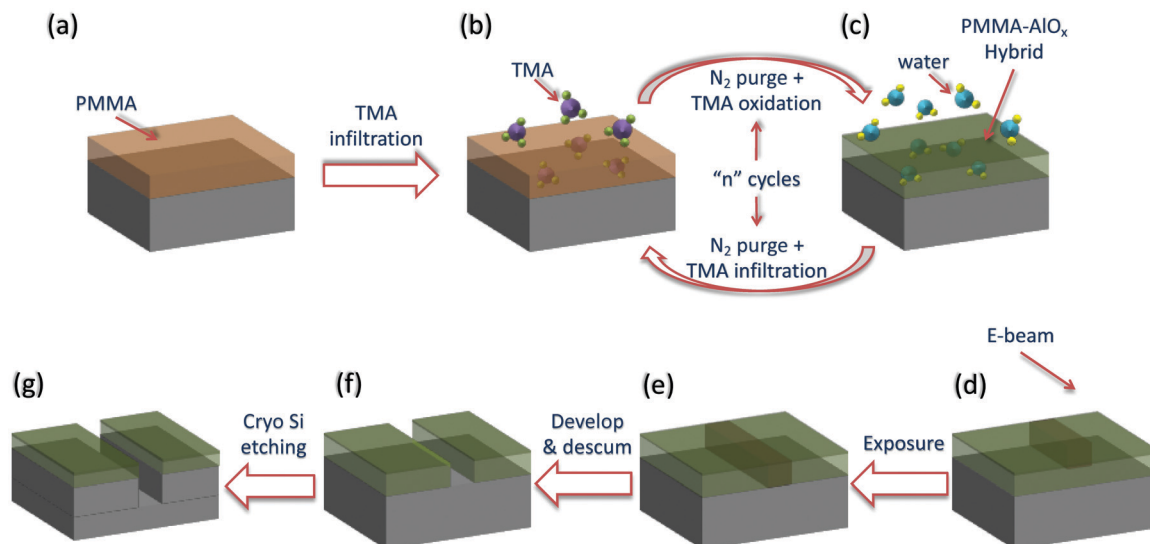


Fig. 1 Schematic representation of the process flow followed during the current study. (a) PMMA 950 A2 was spin coated on cleaned Si substrates at 7500 rpm for 60 s resulting in a ~ 60 nm thick PMMA film. During the infiltration process alternating half-cycles of (b) TMA infiltration and (c) water infiltration are repeated for a given number of times in order to synthesize the *ex situ* processed hybrid resist composition. The sample with the hybrid resist is then subjected to e-beam exposure (d); and the resulting modified resist with specific patterned areas (e) is then developed in a 1 : 3 MIBK : IPA solution for 45 s followed by 15 s IPA rinse to acquire the patterned substrate (f). After an appropriate descum process, the patterned substrate is then subjected to the cryogenic Si etch process at -100 °C using a combination of SF_6 - O_2 gas mixture to transfer the pattern to the Si substrate (g).

an infiltration cycle. In the subsequent half-cycle, an oxidizing precursor, typically water (H_2O), is introduced in a similar way to oxidize the infiltrated TMA, and then purged out. These two combined half-cycles constitute a full infiltration cycle and are repeated several times to achieve the required amount of infiltration of AlO_x in the PMMA matrix (Fig. 1a–c). While the infiltration synthesis technique has previously been reported, we have used a modified version of the same, a micro-dose protocol, where the precursor (or oxidant) is pulsed multiple times during the half cycle exposure to promote a more homogeneous, higher amount of infiltration as we have reported recently.⁸⁰

Although the infiltration synthesis process is based on the ALD tool and uses ALD precursors, the underlying mechanism is vastly different from the normal ALD. In a typical material deposition by ALD, TMA molecules are adsorbed on the substrate surface to form a monolayer during the first half-cycle. This adsorbed layer is subsequently oxidized to form a monolayer of AlO_x , during the second half-cycle. As the cycle is repeated for a given number of times, an AlO_x film is slowly grown on the top of the substrate. In a nutshell, the ALD process is governed by the surface adsorption process. In contrast, during the infiltration half-cycle, which is typically much longer compared to the ALD half-cycle (*i.e.*, a few minutes *vs.* a few seconds), TMA diffuses into the molecular-scale pores available in the PMMA matrix and attaches itself to the carbonyl groups inside the polymeric chains.^{78,81} During the water half-cycle, these TMA molecules are then oxidized to form Al-OH groups. On repeating the infiltration cycle, AlO_x grows on top of the initial Al-OH groups. Ultimately, the total number of applied infiltration cycles thus governs the amount of inorganic or the degree of hybridization of the polymeric matrix.⁷⁷

Results and discussion

We first studied the basic characteristics of our hybrid resist, sensitivity (S) and contrast (γ), where the resist formulation was altered with different numbers of AlO_x infiltration cycles ranging from 0 to 8. We demonstrate an excellent controllability of S and γ based on the amount of infiltration. Particularly, in comparison to the original PMMA resist, we have achieved almost an order of magnitude increase in the contrast. Fig. 1d–f depict the general process of EBL which is employed for resist patterning. Fig. 2a–c show a typical electron dose test carried out in the form of an exposure matrix for uninfiltrated, 4-cycle infiltrated, and 8-cycle infiltrated PMMA, respectively, depicted as the height maps acquired using atomic force microscopy (AFM). The exposure dose in these tests was increased from left to right and top to bottom (the exposure dose used at each array position is included in Table S1, ESI†). The reproducibility of the exposure response of the synthesized hybrid resist was verified using dark-field optical microscopy of the exposure matrix, as shown in Fig. S1 (ESI†), across three or more samples. Consequently, AFM analysis was conducted on a representative sample under each infiltration condition, and the acquired AFM height maps for all the infiltration conditions investigated in this study are shown in Fig. S2 (ESI†). From the AFM maps themselves, it can be observed that the electron dose required to cause a solubility change within the resist and consequently develop positive-tone patterns, increases with the increasing number of infiltration cycles and, thus, the amount of incorporated inorganic content. Based on the prior understanding of the infiltration mechanism, the infiltrated AlO_x growing within the polymer matrix may be causing internal crosslinking among the polymer chains. Similarly, the enhancement

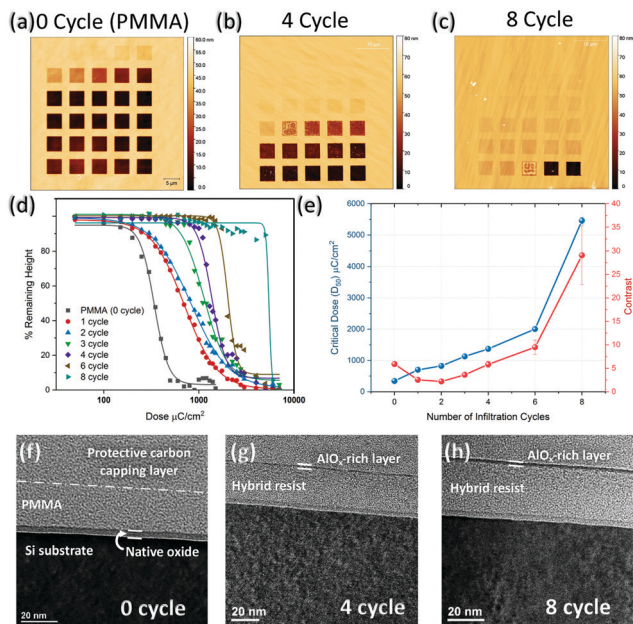


Fig. 2 AFM height maps of the exposure dose matrix patterned as per the dose array shown in Table S1 (ESI[†]) on (a) PMMA (0-cycle infiltration), (b) the 4-cycle infiltrated hybrid resist and (c) the 8-cycle infiltrated hybrid resist. (d) Exposure dose response curves for the remaining formulations studied and illustrated by plotting % remaining height vs. corresponding exposure dose; heights acquired from the AFM maps. (e) Evolution of the critical dose (D_{50}) and contrast (γ) with increasing number of infiltration cycles. Bright-field cross-sectional TEM images of (f) pure PMMA (0-cycle infiltration) (g) 4 cycle infiltrated and (h) 8 cycle infiltrated resist showing increasing amount of AlO_x in the PMMA matrix, along with growing thickness of the AlO_x -rich top layer.

in the resist contrast can also be noticed from the AFM maps; the thickness change within the exposed areas is initially gradual for the hybrid resists with low numbers of infiltration cycles. However, as the infiltrated inorganic content is increased, a more abrupt change in the height of the exposed regions can be seen, clearly suggesting an increase in the contrast of the resist for higher numbers of infiltration cycles.

Fig. 2d shows the exposure matrix height data in the form of post-development remnant height percentage in the exposed region against the exposure dose on a semi-logarithmic scale. All resist profiles show a typical sigmoidal distribution, where the exposure dose required to remove 50% of the resist height is quantified as the critical dose (D_{50}). We find that the sigmoidal contrast curves shift towards higher exposure doses with increased infiltration, implying the requirement of higher exposure dose to clear the resist from the exposed region. The slopes of the sigmoidal contrast curves can also be observed to become steeper with increased infiltration cycles, signifying an increment in the resist contrast, γ , which can be quantified using the expression,⁸²

$$\gamma = \frac{1}{\log_{10}\left(\frac{D_{100}}{D_0}\right)}$$

where D_0 is the onset dose and D_{100} is the dose to clear the resist. The estimated values of critical dose and contrast are plotted

against the number of infiltration cycles in Fig. 2e. A nearly monotonous increase in the critical dose is seen with increased infiltration. The contrast values on the other hand show only a small change until 4 cycles, and rapidly increases to ~ 30 for resists with 8 cycles of infiltration, which is almost a six-fold increase compared to the starting PMMA resist.

In order to investigate the origin of this unexpected contrast enhancement, we conducted cross-sectional transmission electron microscopy (TEM) on the hybrid resist thin films after different amounts of AlO_x infiltration, and the acquired images are shown in Fig. 2f–h. A dense, AlO_x -rich thin layer can be seen to have formed at the top surface of the infiltrated resist, which seems to be getting thicker with increasing amount of infiltration. The formation of such a thin top layer would explain the contrast enhancement in the case of highly infiltrated hybrid resists. Since this top layer can initially retard the developer solution from entering the interior of exposed regions, only a relatively small quantity of the resist would be removed at lower doses, causing an insignificant change in the resist thickness. Such a negligible thickness change would continue until the dose is significantly increased such that a more significant amount of resist under the dense layer starts getting dissolved. When the dose is finally over the critical value, the underlying resist would be completely removed along with the thin top AlO_x -rich layer, consequently rendering the entire exposed region clear. During the height measurement, this is recorded as a sudden removal of all the resist in the exposed region close to a particular exposure dose and translates into a near ideal, high contrast. It should also be noted that the formation of such a top dense layer is typically seen in previous reports of vapor-phase infiltration under the limited diffusion of the AlO_x precursor into the polymer matrix.^{77,83} However, due to the use of a modified micro-dose protocol, we were able to infuse AlO_x much more efficiently throughout the polymer matrix, as indicated by the negligible AlO_x segregation in the PMMA matrix observed in the TEM images, and the thin top layer is likely generated by the adsorption-driven material deposition *via* the standard ALD on the resist surface, which becomes dominant as the molecular pores are being clogged with repeated infiltration cycles.

As the semiconductor industry is marching towards higher and higher device density, the requirement of robust high-resolution patterns is quintessential for advanced nodes. Here, we have used the 4-cycle AlO_x -infiltrated PMMA resist composition and have successfully demonstrated a number of sub-micrometre periodic line and elbow patterns down to 50 nm. Fig. 3a shows a low-magnification scanning electron microscopy (SEM) image of nanopatterns with different linewidths (LWs) and spacings. Fig. 3b shows high-magnification SEM micrographs of 100 nm LW patterns with different periodicity, whereas Fig. 3c shows a magnified image of 1:5 line/space (L/S) patterns of 100 nm LW. Furthermore, elbow patterns of 500 nm half-pitch and 100 nm LW elbow patterns with 500 nm pitch are shown in Fig. 3d and e, respectively. We note that, after the development a descum step was necessary to clear up the remaining residue. While a 10 s O_2 reactive ion etching (RIE) at 100 mTorr pressure and 20 W RF

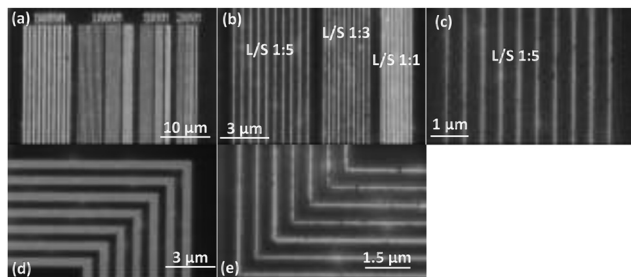


Fig. 3 (a) Low magnification scanning electron microscopy (SEM) image of nanopatterns with LW and spacings. (b) High-magnification SEM micrograph of 100 nm LW patterns with spacing varying from 100 nm to 500 nm. (c) Magnified image of 1:5 line/space patterns of 100 nm LW. (d) Elbow patterns of 500 nm half-pitch and (e) 100 nm LW elbow patterns with 500 nm pitch.

power as a descum protocol is quite commonly used in the case of PMMA-based nanopatterning, we used a 5 s dip in 0.26 N tetramethyl ammonium hydroxide (TMAH) to remove the inorganic residue prior to the O₂ RIE descum step. While the primary purpose of the TMAH dip is to clear residues from the developed region, we note that it may also dissolve the thin AlO_x-rich surface layer on top of unpatterned resist areas. However, the brief TMAH dip does not affect AlO_x retained within the polymer matrix and, thus, the enhanced etch resistance of the hybrid resist. With the help of these high-resolution hybrid resist patterns with high etch

resistance, ultimately, high-aspect-ratio Si patterns could be realized using the plasma-based Si etching processes as discussed below.

In order to transfer developed resist patterns, we have exploited inductively coupled plasma (ICP)-RIE etching using SF₆/O₂-based fluorine chemistry, along with a cryogenic cooling of the substrate down to -100 °C (Fig. 1g). SF₆ provides a very high isotropic etch rate with Si, quite often very hard to control by itself and leading to undercut or pattern broadening. However, such a detrimental sidewall etching can be avoided by inclusion of an appropriate amount of O₂ into the gas mixture. O₂ forms a thin oxyfluoro-polymer (SiO_xF_y) layer as the etching progresses and protects the Si surface.^{84,85} Although this could lead to a significant decrease in the etch rate, due to the ion bombardment directed by the RF bias, the polymer at the bottom of the trench is removed and SF₆ etching can keep progressing at a rapid rate. Additionally, the cryogenic temperature plays a vital role in minimizing the physical erosion of the resist, thus allowing deep high-aspect ratio Si etching.

We have utilized the 4-cycle infiltrated resist formulation to pattern Si nanostructures with a very high aspect ratio of ~17 with a LW of ~30 nm and the depth in excess of 530 nm. Fig. 4a–d depict 60°-tilted SEM images of the high aspect ratio Si structures patterned using the 4-cycle infiltrated PMMA-AlO_x hybrid resist and the SF₆-based cryo-etch for merely 20 s. Low- and high-magnification SEM images of 500 nm half-pitch, high-density patterns are shown in Fig. 4a and b, respectively,

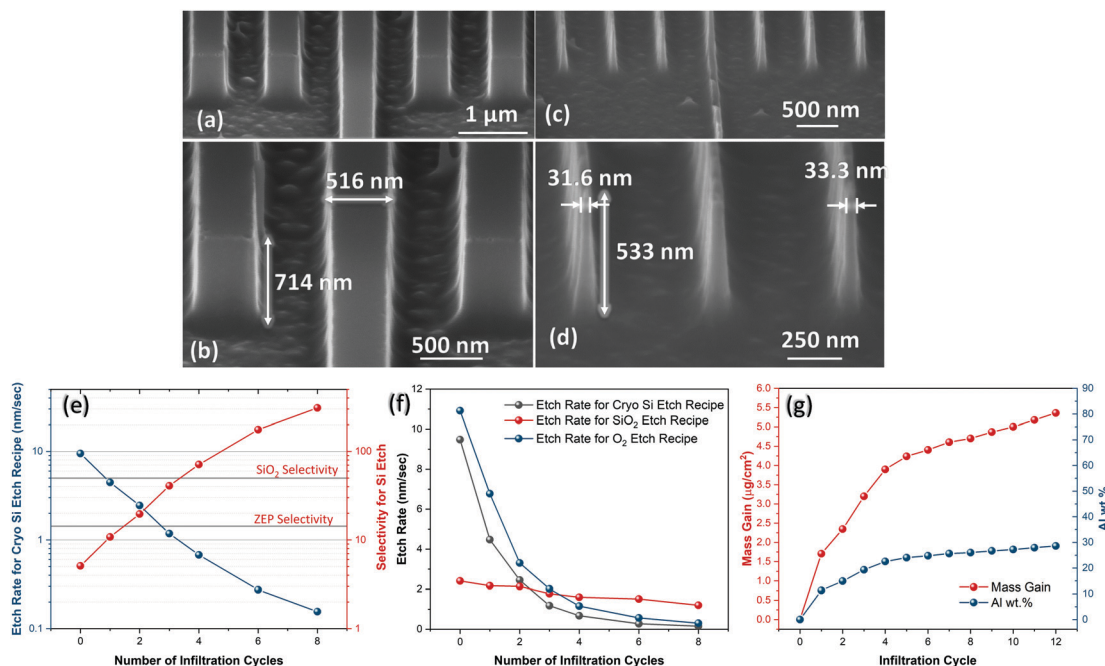


Fig. 4 60°-tilted SEM images of the high aspect ratio Si nanostructures etched using a 4-cycle infiltrated PMMA-AlO_x hybrid resist. (a) Low-magnification and (b) high-magnification SEM images of 500 nm half-pitch high density (1:1 L/S) patterns. (c) Low-magnification and (d) high-magnification SEM images of high-resolution high-aspect-ratio Si nanostructures patterned at 500 nm pitch. (e) Variation in the resist etch rate for the cryo-Si etch process and selectivity for Si etching for resist composition consisting of a different number of infiltration cycles. Notably the 2-cycle infiltrated resist surpasses the selectivity of ZEP and 4-cycle infiltration leads to selectivity higher than the SiO₂ hard mask. (f) A comparison of the decrease in the etch rate with increasing number of infiltration cycles; while a moderate etch rate decrease is seen in the physical etch dominated SiO₂ etch recipe, the decrease in the etch rate for etch recipes with higher chemical component is relatively greater. (g) Mass gain per area (left axis) and Al wt.% (right axis) with increasing number of infiltration cycles estimated *via* QCM measurements.

Table 1 Comparison of various EBL resist processes and their properties. SIS refers to sequential infiltration synthesis

Resist	Lithography	Post lithography treatment	LW (nm)	Etched depth (nm)	Aspect ratio	Dose ($\mu\text{C cm}^{-2}$) [$^*\text{J cm}^{-2}$]	Etch recipe	Resist etch rate (nm min^{-1})	Si etch rate (nm min^{-1})	Selectivity with Si
PMMA ^{78,79}	EBL		20	10	0.5	~ 500	HBr	300	100	3
PMMA ⁷⁹	EBL	SIS	18	130	7.22		HBr	< 4	100	> 25
PMMA ⁷⁸	EBL	SIS	~ 150	1500	~ 10		HBr	~ 8	100	~ 12.5
ZEP520A ⁷⁸	EBL						HBr	100	100	1
ZEP520A ⁷⁸	EBL	SIS					HBr	20	100	5
Al-Si complex ⁴⁸	Soft X-ray (negative)	100 °C for 60 s	400	3300	8.5–17.5	20*	SF ₆ -C ₄ F ₈ -Ar	2.67	170	> 60
Al-Si complex ⁵⁶	EBL 3 kV (negative)		20	400	20	200–250	SF ₆ -C ₄ F ₈ -Ar	2.67	170	> 100
Al-Si complex ⁴⁶	EBL (Dual) 30 kV		< 100 , 20 min	3000	> 30	800	SF ₆ -C ₄ F ₈ -Ar	~ 1.7	170	100
HSQ ⁴⁶	EBL neg		10			5000	SF ₆ -C ₄ F ₈ -Ar		170	6
This work; 4-cycle hybrid	EBL 100 kV		31.6	533	16.87	~ 2000	SF ₆ -O ₂ -cryo	40.67	~ 2895	~ 71.2

while the SEM images of higher-resolution Si structures using the resist patterned at 500 nm pitch are shown in Fig. 4c and d. The LW of ~ 31.6 nm and depth of 533 nm leading to the aspect ratio as high as 16.8 was thus achieved.

In an attempt to benchmark our resist's performance against previously reported resists, we have summarized key performance parameters in Table 1. While etched structures with the aspect ratio as high as 100 have been previously reported by Brusatin *et al.*,⁴⁶ it should be noted that the inorganic content infiltrated in our resist is significantly lower, and the infiltrated AlO_x has fundamentally altered the chemical nature of the PMMA resists generating a hybrid nanocomposite, which has in turn increased its robustness for plasma etching. Such an unprecedented enhancement of the polymer mechanical properties due to AlO_x-infiltration has also been previously reported in the case of a SU-8 resist.⁸⁶ Moreover, organo-silane chemistry based resists reported by Brusatin *et al.* show susceptibility to ambient humidity,⁵⁰ which compromises their long-term shelf life. Tseng, Elam, Darling *et al.*, in their original reports demonstrating the process of infiltration synthesis for etch resistance improvement of patterned PMMA and ZEP resist structures, utilized infiltration after the initial patterning step,^{78,79} demonstrating the Si etch selectivity of over 25 for HBr chemistry.

In comparison, in our *ex situ*-generated PMMA-AlO_x hybrid resists not only is selectivity as high as ~ 309 estimated, but also having a pre-infiltrated resist imparts improved robustness and allows usability of rather thicker resist films without causing pattern collapse. The Si etch selectivity demonstrated by our process also surpasses the routinely used resist, ZEP (selectivity ~ 14.3 for our cryo Si recipe and ~ 1 for HBr chemistry⁷⁸) and HSQ (~ 6 for SF₆-C₄F₈-Ar chemistry;⁴⁶ the detailed list of resists/hard mask tested in this study is provided in Table 2). Moreover, while we have utilized the hybrid resist with 4-cycle infiltration (selectivity ~ 70) for demonstrating nanostructures and pattern transfer, the extrapolation of the measured resist etch rate data suggests that Si etch selectivity more than 300 should be achievable by further increasing the amount of infiltration up to 8 cycles. The variation in Si etch selectivity for our cryo etch process based on the number of infiltration cycles is shown in Fig. 4e. The trend of selectivity improvement with increasing infiltration also demonstrates easy controllability of the resist's robustness for etching based processing. After merely 2-cycles of infiltration, the etch selectivity exhibited by the hybrid resist (~ 20) surpasses that of the ZEP resist (~ 14.3), which, albeit being costly, is a popular choice for etching based pattern transfer. In a number of industrial processes, an SiO₂ hard mask is employed between the resist and the Si substrate, in order to improve the selectivity at the expense of a few additional steps.⁷⁹ It should be noted that our 4-cycle infiltrated hybrid resist formulation shows 40% higher Si etch selectivity (~ 70) as compared to thermal SiO₂ (~ 50), thus removing the need for additional processing steps.

In order to elucidate the effect of hybridization on various aspects of the ICP-RIE etching process, we selected three different etch recipes with each having different degrees of combined chemical and physical etching characteristics. The cryo-Si etch

Table 2 Summary of measured resist/hard-mask etching rate for the cryo-Si etching process and corresponding estimated selectivity for Si etch

Resist/hard mask material	Etch rate (nm min ⁻¹)	Selectivity with Si etching
SiO ₂	58.0	49.9
ZEP520	202.2	14.3
PMMA	568.6	5.1
PMMA–AlO _x hybrid, 1 cycle	268.3	10.8
PMMA–AlO _x hybrid, 2 cycle	147.2	19.7
PMMA–AlO _x hybrid, 3 cycle	70.7	40.9
PMMA–AlO _x hybrid, 4 cycle	40.7	71.2
PMMA–AlO _x hybrid, 6 cycle	16.5	175.9
PMMA–AlO _x hybrid, 8 cycle	9.4	309.2

recipe, utilized for the aforementioned high aspect ratio Si etching, contains both physical and chemical components that play roles in the etching process. A pure O₂ etch is typically used predominantly for removing the organic resist and proceeds *via* the chemical route, whereas, the SiO₂ etch recipe majorly relies on the physical sputtering aspect. As shown in Fig. 4f, for all three etching recipes, there is a decrease in the etching rate with increasing number of infiltration cycles. Interestingly though, the change in the etch rate for cryo-Si and O₂ etch recipes, is much more drastic compared to the observed change in the etch rate for the SiO₂ etching recipe. This observation is rather surprising considering that the common predisposition behind the inclusion of inorganic components into the organic matrix is to improve their resistance to physical damage caused by sputtering when subjected to plasma. In contrast, our hybrid resists seem to show comparatively higher chemical resistance than physical resistance, indicating that our process has altered the chemical nature of the original polymer matrix.

We further estimated the amount of AlO_x infiltrated into the PMMA matrix with the help of quartz crystal microbalance (QCM) measurements (temporal frequency variation shown in Fig. S3, ESI†), and the resulting areal mass gain for different number of infiltration cycles is shown in Fig. 4g. It can be noticed that initially the mass gain rate is relatively high, but it starts decreasing as the infiltration cycles repeat. Such a trend in the mass gain behaviour is attributed to the fact that the number of reactive sites within the PMMA matrix decreases with each infiltration cycle and thus for higher cycles, the TMA molecule could not find sufficient reactive sites to form chemical bonds. Additionally, the formation of a thin top AlO_x-rich layer also should be contributing to the decreasing permeability of the TMA molecules. The evolution of Al wt% with increasing number of infiltration cycles is also shown in Fig. 4g. It is noteworthy that ~30 wt% of Al could be infiltrated into the PMMA matrix (at 12 cycles) with the corresponding Al/C atomic ratio of ~0.3 (Fig. S4, ESI†).

Controllability of the resist performance is a unique aspect of our resist system that makes it a versatile resist platform. Depending upon the end application in mind, the resist formulation could be easily altered to achieve an optimal performance of the resist. For example, the cutting-edge Fin-FET based transistor architecture used in the latest processor chips requires patterning down to sub-10 nm with the device height

being ~50 nm. Low amount of infiltration can provide high throughput high resolution patterning with relatively low aspect ratio patterns, as needed in this case. On the other hand, the memory device industry is exploiting three-dimensional (3D) stacking of the memory cells in order to increase the memory density, where rather lower LW resolution (~100 nm) suffices, but with the required etch depth as high as a few micrometres. Increasing the amount of infiltration can give an ultra-high contrast and extremely high aspect ratio with some decrease in the throughput and relatively lower resolution, which is quite suitable for the posed requirement.

While the current work has majorly focused on the EBL of the PMMA–AlO_x hybrid resist, our resist platform in principle can easily be adaptable for other advanced lithography techniques. Starting this year, a number of leading semiconductor manufacturers are embarking towards utilizing EUV lithography (EUVL), which has been in the research pipeline for more than a decade. EUVL, owing to its ultra-short wavelength, can pattern sub-10 nm structures in single exposures, which would obviate the need for multi-patterning strategies and decrease design complexity. The current understanding of the EUVL exposure mechanism in resists is that the interaction of EUV photons with resists gives rise to secondary photoelectrons that can carry out the solubility change within the resist.^{1,87} Moreover, the absorption of EUV radiation is primarily realized by the component atoms, and thus the inclusion of specific elements in the resist formulation has significant impacts. For instance, metal atoms such as Al show relatively high EUV absorption, while metals like Sn can exhibit very high EUV absorption,^{88,89} compared with carbon, hydrogen, and oxygen, the primary atomic components of pure organic resists, which have low EUV absorption. That said, although, the current study has primarily focused on AlO_x infiltration into the polymer matrix, the ease of processing and controllability of our hybrid resist make it a versatile, potential route towards generating organic–inorganic hybrid resists containing other metal and metal oxide systems^{77,90–96} for high-throughput patterning of the sub-10 nm structure with required high aspect ratios *via* EUVL. Moreover, we note that further investigation to explore resist and infiltration synthesis chemistries as well as developer chemistries and protocols may prove beneficial for optimizing key resist performance parameters such as sensitivity and line edge roughness (LER).

Conclusions

In summary, we have developed a new, high-performance, easy-to-access hybrid resist system, *via* the *ex situ* infiltration synthesis process based only on existing standard materials and tools. Implementing our resist strategy with a representative system based on PMMA and AlO_x, we have achieved a very high contrast of ~30 for EBL-based patterning, with a minor increase in the required exposure dose, which is still similar to widely used negative-tone resist HSQ. Moreover, we have been able to demonstrate the fabrication of Si nanopatterns with a high aspect ratio of ~17 owing to the etch selectivity value of ~71.2, much higher (5–14 times higher) than

commonly used resists, such as PMMA, ZEP and HSQ. Another four-fold increment in the selectivity (reaching >300) is also estimated for the hybrid infiltrated with 8 infiltration cycles. By subjecting our resists to different plasma-RIE processes, we also uncovered unique enhancement in the chemical etch resistance. Since there is no complex underlying chemical synthesis requirement, the process is extremely easy to implement and modify. Versatile controllability of the generated hybrid resist performance is yet another highly desirable attribute, suitable for optimal process development as per the application demand. Moreover, with the industry advancing to EUVL for HVM, our technique should be also utilizable, with appropriate choices of infiltrated inorganic elements, towards achieving high throughput nanolithography for next generation electronics development.

Experimental methods

Hybrid resist formulation by infiltration synthesis

Commercially available 2 wt% PMMA (molecular weight 950 000 g mol⁻¹ – MicroChem) in anisole was spin coated on cleaned silicon substrates at 7500 rpm for 60 s, followed by 3 min baking at 180 °C on a hotplate to form an ~60 nm film as measured by ellipsometry. The substrates with as spun PMMA film were then infiltrated at 85 °C with different amounts of AlO_x by varying the number of infiltration cycles from 1–12 using a commercial ALD system (Cambridge Nanotech Savannah S100). Each infiltration cycle consisted of TMA exposure for a total of 60 s, during which the TMA precursor was pulsed for 14 ms every 10 s, followed by purging of the ALD chamber with 100 sccm N₂ for 2 min. Consequently, the substrates were exposed to water vapor for a total of 60 s, while the 40 ms pulse was employed every 10 s, followed by 2 min purge by 100 sccm N₂, completing the infiltration cycle.

EBL

E-beam exposure on the prepared samples was carried out using the JEOL JBX-6300FS EBL system (100 kV). For the exposure matrix patterning typically 500 pA current was used to expose a 5 μm square area with electron dose ranging from 50 μC cm⁻² to 7000 μC cm⁻² using a shot spacing of 8 nm. For exposing sub-micrometer scale features consisting of lines and elbow patterns 1 nA beam current and 4 nm shot spacing were used (exposure dose range differed for various formulations). After exposure, samples were developed in methyl iso-butyl ketone (MIBK) solution in isopropyl alcohol (IPA) in a ratio of MIBK: IPA 1:3 for 45 s followed by 15 s rinse in IPA.

Dry etching

All ICP-RIE processing was conducted on an Oxford Plasmalab 100. The plasma processing conditions are summarized in Table S2 (ESI[†]).

Electron microscopy characterization

SEM micrographs were acquired using a Hitachi 4800 field-emission SEM. Cross-sectional TEM samples were prepared by

a standard *in situ* lift-out procedure using Ga ion milling in a focused ion beam system (FEI Helios 600 Nanolab). TEM images were taken using a JEOL JEM-1400 TEM at 120 kV. AFM characterization of the dose test measurements was carried out using a Park NX20 AFM with PPP-NCHR tips.

Conflicts of interest

There are no conflicts to declare.

Acknowledgements

The authors thank Dr Xiao Tong for his assistance with AFM measurements and Dr Dmytro Nykypanchuk for ellipsometry measurements. The research was carried out at the Center for Functional Nanomaterials (CFN), Brookhaven National Laboratory (BNL), which is supported by the U.S. Department of Energy, Office of Basic Energy Sciences, under Contract No. DE-SC0012704.

References

- 1 S. Wang, L. Li, C. K. Ober, E. P. Giannelis, X. Liu and S. Pal, *Chem. Soc. Rev.*, 2017, **46**, 4855–4866.
- 2 E. P. Giannelis, M. Trikeriotis, R. Rodriguez, W. J. Bae, M. F. Zettel, C. K. Ober, E. Piscani and P. Zimmerman, *Adv. Resist Mater. Process. Technol. XXVI*, 2009, **7273**, 727326.
- 3 M. A. Morris, *Microelectron. Eng.*, 2015, **132**, 207–217.
- 4 J. Roberts, R. A. Griffiths, A. Vijayaraghavan, T. Thomson, A. Williams and C. Oakland, *J. Phys. D: Appl. Phys.*, 2013, **46**, 503001.
- 5 R. F. Pease and S. Y. Chou, *Proc. IEEE*, 2008, **96**, 248–270.
- 6 L. Li, S. Chakrabarty, K. Spyrou, C. K. Ober and E. P. Giannelis, *Chem. Mater.*, 2015, **27**, 5027–5031.
- 7 A. Tavakkoli, K. G., S. N. Piramanayagam, M. Ranjbar, R. Sbiaa and T. C. Chong, *J. Vac. Sci. Technol., B: Nanotechnol. Microelectron.: Mater., Process., Meas., Phenom.*, 2011, **29**, 011035.
- 8 M. A. Hartney, R. R. Kunz, D. J. Ehrlich and D. C. Shaver, in *Advances in Resist Technology and Processing VII*, ed. M. P. C. Watts, 1990, vol. 1262, p. 119.
- 9 J. W. Thackeray, *J. Vac. Sci. Technol., B: Microelectron. Nanometer Struct.–Process., Meas., Phenom.*, 1989, **7**, 1620.
- 10 M. Endo, I. Satou, H. Watanabe and H. Morimoto, *Microelectron. Eng.*, 2000, **53**, 485–488.
- 11 E. K. Pavelchek, *J. Vac. Sci. Technol., B: Microelectron. Nanometer Struct.–Process., Meas., Phenom.*, 1990, **8**, 1497.
- 12 R. S. Hutton, *J. Vac. Sci. Technol., B: Microelectron. Nanometer Struct.–Process., Meas., Phenom.*, 1990, **8**, 1502.
- 13 B. Roland, *Microelectron. Eng.*, 1991, **13**, 11–18.
- 14 C. Pierrat, S. Tedesco, F. Vinet, T. Mourier, M. Lerme, B. Dal'Zotto and J. C. Guibert, *Microelectron. Eng.*, 1990, **11**, 507–514.
- 15 D. Kontziampasis, K. Beltsios, E. Tegou, P. Argitis and E. Gogolidis, *J. Appl. Polym. Sci.*, 2010, **117**, 2189–2195.

- 16 K. Arshak, M. Mihov, A. Arshak, D. McDonagh, M. Pomeroy and M. Champion, *Microelectron. Eng.*, 2002, **61–62**, 783–791.
- 17 M. Ryoo, S. Shirayone, E. Yano, S. Okazaki and S. Kang, *Microelectron. Eng.*, 2002, **61–62**, 723–728.
- 18 A. Sinha, D. W. Hess and C. L. Henderson, *Electrochem. Solid-State Lett.*, 2006, **9**, G330.
- 19 P. A. F. Herbert, J. Braddell and S. Mackenzie, *Engineering*, 1994, **23**, 263–266.
- 20 F. E. Prins, J. Pfeiffer, S. Raible, D. P. Kern and V. Schurig, *Microelectron. Eng.*, 1998, **42**, 359–362.
- 21 K. Arshak, M. Mihov, D. Sutton, A. Arshak and S. B. Newcomb, *Microelectron. Eng.*, 2003, **67–68**, 130–139.
- 22 K. Kasahara, C. K. Ober, H. Xu, V. Kosma and J. Odent, *J. Micro/Nanolithogr., MEMS, MOEMS*, 2017, **16**, 1.
- 23 C. Y. Ouyang, Y. S. Chung, L. Li, M. Neisser, K. Cho, E. P. Giannelis and C. K. Ober, in *Advances in Resist Materials and Processing Technology XXX*, ed. M. H. Somervell, 2013, vol. 8682, p. 86820R.
- 24 C. K. Ober, M. Trikeriotis, S. Chakrabarty, C. Ouyang, M. Kryask and E. P. Giannelis, *J. Photopolym. Sci. Technol.*, 2013, **26**, 659–664.
- 25 L. Li, S. Chakrabarty, J. Jiang, B. Zhang, C. Ober and E. P. Giannelis, *Nanoscale*, 2016, **8**, 1338–1343.
- 26 P. G. Reddy, N. Mamidi, P. Kumar, S. K. Sharma, S. Ghosh, K. E. Gonsalves and C. P. Pradeep, *RSC Adv.*, 2016, **6**, 67143–67149.
- 27 E. C. Mattson, Y. Cabrera, S. M. Rupich, Y. Wang, K. A. Oyekan, T. J. Mustard, M. D. Halls, H. A. Bechtel, M. C. Martin and Y. J. Chabal, *Chem. Mater.*, 2018, **30**, 6192–6206.
- 28 M. Sortland, J. Hotalen, R. Del Re, J. Passarelli, M. Murphy, T. S. Kulmala, Y. Ekinici, M. Neisser, D. A. Freedman and R. L. Brainard, *J. Micro/Nanolithogr., MEMS, MOEMS*, 2015, **14**, 043511.
- 29 M. Murphy, S. Grzeskowiak, J. Sitterly, G. H. Denbeaux and R. L. Brainard, *Proc. SPIE*, 2018, **10586**, 1058608.
- 30 M. Murphy, A. Narasimhan, S. Grzeskowiak, J. Sitterly, P. Schuler, J. Richards, G. Denbeaux and R. L. Brainard, *Extrem. Ultrav. Lithogr. VIII*, 2017, **10143**, 1014307.
- 31 S. Grzeskowiak, A. Narasimhan, M. Murphy, L. Napolitano, D. A. Freedman, R. L. Brainard and G. Denbeaux, *Adv. Patterning Mater. Process. XXXIV*, 2017, **10146**, 1014605.
- 32 J. Haitjema, Y. Zhang, M. Vockenhuber, D. Kazazis, Y. Ekinici and A. M. Brouwer, in *Extreme Ultraviolet (EUV) Lithography VIII*, ed. E. M. Panning and K. A. Goldberg, 2017, vol. 10143, p. 1014325.
- 33 J. Haitjema, T. A. Jung, D. Kazazis, A. M. Brouwer, Y. Ekinici, M. Vockenhuber, M. Baljovic and Y. Zhang, *J. Photopolym. Sci. Technol.*, 2018, **31**, 249–255.
- 34 D. J. Webb and M. Hatzakis, *J. Vac. Sci. Technol.*, 1979, **16**, 2008–2013.
- 35 K. Yamaguchi, *J. Electrochem. Soc.*, 1992, **139**, L33.
- 36 M. Nedelcu, M. S. M. Saifullah, D. G. Hasko, A. Jang, D. Anderson, W. T. S. Huck, G. A. C. Jones, M. E. Welland, D. J. Kang and U. Steiner, *Adv. Funct. Mater.*, 2010, **20**, 2317–2323.
- 37 K. R. V. Subramanian, M. S. M. Saifullah, E. Tapley, D. J. Kang, M. E. Welland and M. Butler, *Nanotechnology*, 2004, **15**, 158–162.
- 38 M. S. M. Saifullah, K. R. V. Subramanian, E. Tapley, D. J. Kang, M. E. Welland and M. Butler, *Nano Lett.*, 2003, **3**, 1587–1591.
- 39 M. S. M. Saifullah, M. Z. R. Khan, D. G. Hasko, E. S. P. Leong, X. L. Neo, E. T. L. Goh, D. Anderson, G. A. C. Jones and M. E. Welland, *J. Vac. Sci. Technol., B: Microelectron. Nanometer Struct.–Process., Meas., Phenom.*, 2010, **28**, 90.
- 40 K. R. V. Subramanian, M. S. M. Saifullah, E. Tapley, D.-J. Kang, M. E. Welland and M. Butler, *Nanotechnology*, 2004, **15**, 158–162.
- 41 M. S. M. Saifullah, H. Namatsu, T. Yamaguchi, K. Yamazaki and K. Kurihara, *1999 Int. Microprocess. Nanotechnol. Conf.*, 1999, **38**, 160–161.
- 42 M. S. M. Saifullah, D.-J. Kang, K. R. V. Subramanian, M. E. Welland, K. Yamazaki and K. Kurihara, *J. Sol-Gel Sci. Technol.*, 2004, **29**, 5–10.
- 43 M. S. M. Saifullah, K. R. V. Subramanian, D. Anderson, D.-J. Kang, W. T. S. Huck, G. A. C. Jones and M. E. Welland, *J. Vac. Sci. Technol., B: Microelectron. Nanometer Struct. – Process., Meas., Phenom.*, 2006, **24**, 1215.
- 44 M. S. M. Saifullah, *Cosmos*, 2009, **05**, 1–21.
- 45 M. S. M. Saifullah, K. R. V. Subramanian, D.-J. Kang, D. Anderson, W. T. S. Huck, G. A. C. Jones and M. E. Welland, *Adv. Mater.*, 2005, **17**, 1757–1761.
- 46 E. Zanchetta, G. Della Giustina, G. Greci, A. Pozzato, M. Tormen and G. Brusatin, *Adv. Mater.*, 2013, **25**, 6261–6265.
- 47 L. Brigo, A. Pistore, G. Greci, A. Carpentiero, F. Romanato and G. Brusatin, *Microelectron. Eng.*, 2010, **87**, 947–950.
- 48 G. Greci, G. Della Giustina, A. Pozzato, E. Zanchetta, M. Tormen and G. Brusatin, *Microelectron. Eng.*, 2012, **98**, 134–137.
- 49 G. Greci, G. Della Giustina, A. Pozzato, G. Brusatin and M. Tormen, *Microelectron. Eng.*, 2011, **88**, 1964–1967.
- 50 A. Cattoni, D. Mailly, O. Dalstein, M. Faustini, G. Seniutinas, B. Rösner and C. David, *Microelectron. Eng.*, 2018, **193**, 18–22.
- 51 R. P. Oleksak, R. E. Ruther, F. Luo, K. C. Fairley, S. R. Decker, W. F. Stickle, D. W. Johnson, E. L. Garfunkel, G. S. Herman and D. A. Keszler, *ACS Appl. Mater. Interfaces*, 2014, **6**, 2917–2921.
- 52 R. P. Oleksak and G. S. Herman, in *Proc. of SPIE*, ed. O. R. Wood and E. M. Panning, 2014, vol. 9048, p. 90483H.
- 53 B. Cui, A. S. Abbas, B. B. Shokouhi, S. Alqarni and M. Yavuz, *Mater. Res. Express*, 2014, **1**, 045102.
- 54 J. Zhang, K. Cao, X. S. Wang and B. Cui, *Chem. Commun.*, 2015, **51**, 17592–17595.
- 55 S. Il Lee, J. H. Sim, H. J. Lee, R. Kasica, H. M. Kim, C. L. Soles, K. B. Kim and D. Y. Yoon, *Appl. Organomet. Chem.*, 2013, **27**, 644–651.
- 56 G. Greci, E. Zanchetta, A. Pozzato, G. Della Giustina, G. Brusatin and M. Tormen, *Appl. Mater. Today*, 2015, **1**, 13–19.
- 57 M. Zhao, B. Chen, C. Xie, M. Liu and J. Nie, *2010 IEEE 5th Int. Conf. Nano/Micro Eng. Mol. Syst. NEMS 2010*, 2010, pp. 1021–1024.

- 58 G. Singh, P. Stenberg, P. Vahima, M. Kuittinen, R. P. Yadav and V. Janyani, *Adv. Fabr. Technol. Micro/Nano Opt. Photonics IV*, 2011, **7927**, 792715.
- 59 A. E. Grigorescu and C. W. Hagen, *Nanotechnology*, 2009, **20**, 292001.
- 60 A. E. Grigorescu, M. C. van der Krogt, C. W. Hagen and P. Kruit, *Microelectron. Eng.*, 2007, **84**, 822–824.
- 61 D. A. Czaplewski and L. E. Ocola, *J. Vac. Sci. Technol., B: Nanotechnol. Microelectron.: Mater., Process., Meas., Phenom.*, 2011, **29**, 021601.
- 62 D. A. Czaplewski, D. R. Tallant, G. A. Patrizi, J. R. Wendt and B. Montoya, *J. Vac. Sci. Technol., B: Microelectron. Nanometer Struct.–Process., Meas., Phenom.*, 2009, **27**, 581.
- 63 S. Thoms and D. S. Macintyre, *J. Vac. Sci. Technol., B: Nanotechnol. Microelectron.: Mater., Process., Meas., Phenom.*, 2014, **32**, 06FJ01.
- 64 M. Schirmer, B. Büttner, F. Syrowatka, G. Schmidt, T. Köpnick and C. Kaiser, *29th Eur. Mask Lithogr. Conf.*, 2013, **8886**, 88860D.
- 65 A. Gerardino, M. Gentili, E. Di Fabrizio, R. Calarco and L. Mastrogiacomio, *Microelectron. Eng.*, 1999, **46**, 201–204.
- 66 S. Kaya, F. Rahman, D. J. Carbaugh, S. G. Pandya and J. T. Wright, *Nanotechnology*, 2017, **28**, 455301.
- 67 S. Yasin, D. G. Hasko and H. Ahmed, *Microelectron. Eng.*, 2002, **61–62**, 745–753.
- 68 S. Gorelick, V. A. Guzenko, J. Vila-Comamala and C. David, *Nanotechnology*, 2010, **21**, 295303.
- 69 Y. Chen, D. Macintyre and S. Thoms, *J. Vac. Sci. Technol., B: Microelectron. Nanometer Struct.–Process., Meas., Phenom.*, 2002, **17**, 2507.
- 70 W. Hu, G. H. Bernstein, K. Sarveswaran and M. Lieberman, *Proc. IEEE Conf. Nanotechnol.*, 2003, **2**, 602–605.
- 71 K. Koshelev, M. Ali Mohammad, T. Fito, K. L. Westra, S. K. Dew and M. Stepanova, *J. Vac. Sci. Technol., B: Nanotechnol. Microelectron.: Mater., Process., Meas., Phenom.*, 2011, **29**, 06F306.
- 72 V. R. Manfrinato, A. Stein, L. Zhang, C. Y. Nam, K. G. Yager, E. A. Stach and C. T. Black, *Nano Lett.*, 2017, **17**, 4562–4567.
- 73 C. Zhang, C. Yang and D. Ding, *J. Micromech. Microeng.*, 2004, **14**, 663–666.
- 74 B. Smith, P. Zimmerman, B. Baylav, R. Yin, T. Smith, C. Scholz, P. Xie and M. Zhao, *Adv. Resist Mater. Process. Technol. XXVII*, 2010, **7639**, 763915.
- 75 M. Wang, N. D. Jarnagin, C. T. Lee, C. L. Henderson, W. Yueh, J. M. Roberts and K. E. Gonsalves, *J. Mater. Chem.*, 2006, **16**, 3701–3707.
- 76 R. D. Peters, G. R. Amblard, J.-J. Lee and T. Guenther, *Adv. Resist Technol. Process. XX*, 2003, **5039**, 393.
- 77 A. Subramanian, N. Tiwale and C.-Y. Nam, *JOM*, 2019, **71**, 185–196.
- 78 Y.-C. Tseng, Q. Peng, L. E. Ocola, D. A. Czaplewski, J. W. Elam and S. B. Darling, *J. Mater. Chem.*, 2011, **21**, 11722.
- 79 Y. C. Tseng, A. U. Mane, J. W. Elam and S. B. Darling, *Adv. Mater.*, 2012, **24**, 2608–2613.
- 80 A. Subramanian, G. Doerk, K. Kisslinger, D. H. Yi, R. B. Grubbs and C.-Y. Nam, *Nanoscale*, 2019, **11**, 9533–9546.
- 81 M. Biswas, J. A. Libera, S. B. Darling and J. W. Elam, *Chem. Mater.*, 2014, **26**, 6135–6141.
- 82 L. Y. M. Tobing, L. Tjahjana and D. H. Zhang, *Nanotechnology*, 2013, **24**, 075303.
- 83 Y. Ozaki, S. Ito, N. Hiroshiba, T. Nakamura and M. Nakagawa, *Jpn. J. Appl. Phys.*, 2018, **57**, 06HG01.
- 84 M. Kulsreshath, A. Vital, P. Lefauchaux, C. Sinturel, T. Tillocher, M. Vayer, M. Boufnichel and R. Dussart, *Micro Nano Eng.*, 2018, **1**, 42–48.
- 85 B. Wu, A. Kumar and S. Pamarthy, *J. Appl. Phys.*, 2010, **108**, 051101.
- 86 K. J. Dusoe, X. Ye, K. Kisslinger, A. Stein, S. W. Lee and C. Y. Nam, *Nano Lett.*, 2017, **17**, 7416–7423.
- 87 R. L. Brainard, M. Neisser, G. M. Gallatin and A. K. Narasimhan, *EUV Lithography, Second Edition*, SPIE, 2018, pp. 493–591.
- 88 R. Fallica, J. Haitjema, L. Wu, S. Castellanos, A. M. Brouwer and Y. Ekinici, *J. Micro/Nanolithography, MEMS, MOEMS*, 2018, **17**, 1.
- 89 R. Fallica, J. Haitjema, L. Wu, S. Castellanos, F. Brouwer and Y. Ekinici, in *Extreme Ultraviolet (EUV) Lithography VIII*, ed. E. M. Panning and K. A. Goldberg, 2017, vol. 10143, p. 101430A.
- 90 J. Kamcev, D. S. Germack, D. Nykypanchuk, R. B. Grubbs, C. Y. Nam and C. T. Black, *ACS Nano*, 2013, **7**, 339–346.
- 91 Q. Peng, Y. C. Tseng, Y. Long, A. U. Mane, S. DiDona, S. B. Darling and J. W. Elam, *Langmuir*, 2017, **33**, 13214–13223.
- 92 X. Ye, J. Kestell, K. Kisslinger, M. Liu, R. B. Grubbs, J. A. Boscoboinik and C. Y. Nam, *Chem. Mater.*, 2017, **29**, 4535–4545.
- 93 L. E. Ocola, A. Connolly, D. J. Gosztola, R. D. Schaller and A. Yanguas-Gil, *J. Phys. Chem. C*, 2017, **121**, 1893–1903.
- 94 C. Z. Leng and M. D. Losego, *Mater. Horiz.*, 2017, **4**, 747–771.
- 95 C.-Y. Nam and A. Stein, *Adv. Opt. Mater.*, 2017, **5**, 1700807.
- 96 J. J. Kim, H. S. Suh, C. Zhou, A. U. Mane, B. Lee, S. Kim, J. D. Emery, J. W. Elam, P. F. Nealey, P. Fenter and T. T. Fister, *Nanoscale*, 2018, **10**, 3469–3479.